



# Nonlinear dynamics analysis of high contact ratio gears system with multiple clearances

Kang Huang<sup>1</sup> · Yong Yi<sup>1</sup> · Yangshou Xiong<sup>2,3</sup> · Zhenbang Cheng<sup>1</sup> · Huan Chen<sup>4</sup>

Received: 22 August 2019 / Accepted: 10 January 2020 / Published online: 25 January 2020  
© The Brazilian Society of Mechanical Sciences and Engineering 2020

## Abstract

A brief research status on high contact ratio gears (HCRG) is first conducted to obtain a basic understanding. Subsequently, a nonlinear dynamic model of HCRG with multiple clearances is established by the lumped mass method, in which time-varying mesh stiffness (TVMS), static transmission error, gear backlash, and bearing radial clearance are taken into consideration as well. The TVMS of HCRG is calculated based on an improved potential energy model and then fitted into a Fourier series form. After the dimensionless treatment, the system differential equations of motion are solved using Runge–Kutta numerical integration method. With the help of bifurcation diagrams, largest Lyapunov exponent charts, time-domain waveforms, FFT spectra, Poincaré maps, and phase diagrams, the influence of excitation frequency, gear backlash, mesh damping ratio, error fluctuation, and bearing radial clearance on the nonlinear dynamic characteristics of the system is investigated in detail. The results show that with the changes of these analysis parameters, the system exhibits different types of nonlinear behaviors and dynamic evolution mechanism, including period-one, multi-periodic, quasi-periodic, chaotic motions, and jump discontinuity phenomenon. Meanwhile, three typical routes to chaos, namely period-doubling bifurcation to chaos, quasi-period to chaos, and crisis to chaos, are also demonstrated. Additionally, it is found that the bearing radial clearance produces a weaker nonlinear coupling effect when compared to gear backlash. The research results can provide a certain theoretical support for the dynamic design and vibration control of the HCRG.

**Keywords** HCRG · TVMS · Bifurcation · Chaos · Gear backlash · Bearing radial clearance

## 1 Introduction

High contact ratio gears (HCRG) are generally referred as a spur gear mesh with a contact ratio between two and three. This means there are at least two tooth pairs in contact at all times during the gear mesh, whereas conventional low contact ratio gears (LCRG) alternate between one and two

pairs in contact [1]. HCRG have been received much concern especially in the military application fields, because they have the advantages of higher power-to-weight ratio, higher load-carrying capacity, smoother running, and lower noise attributes, etc. [2, 3].

Though HCRG have many significant advantages, it would be expected that HCRG would be more sensitive to tooth spacing errors and tooth profile modifications because of the multiple tooth contacts. In the past few decades, most of research on HCRG has mainly been concentrated on tooth load sharing, stress analysis, and tooth profile modification. Staph [4] discussed the effects of gear parameters on several performance factors of HCRG and gave a method to tooth load sharing in HCRG. Cornell and Westervelt [1] developed a dynamic model for calculating the dynamic tooth loads and root stresses for HCRG. Based on the compliance equations of the loaded teeth, Rosen and Frint [2] presented an analytical method to calculate the HCRG tooth load sharing. Similar methods were also adopted by Elkholy [5], Tavakoli and Houser [6], and Mohanty [7]. Wang and Howard [8]

---

Technical Editor: Pedro Manuel Calas Lopes Pacheco, D.Sc.

✉ Yangshou Xiong  
xiongys@hfut.edu.cn

<sup>1</sup> School of Mechanical Engineering, Hefei University of Technology, Hefei 230009, China

<sup>2</sup> Institute of Industry and Equipment Technology, Hefei University of Technology, Hefei 230009, China

<sup>3</sup> Anhui Province Key Lab of Aerospace Structural Parts Forming Technology and Equipment, Hefei 230009, China

<sup>4</sup> HRG Institute (Hefei) of International Innovation, Hefei 230601, China

used finite element analysis (FEA) to calculate the load sharing ratio, contact stress and the maximum tooth root stress of HCRG. Rameshkumar [3] studied the load sharing ratio, bending stress, contact stress, and deflection for LCRG/HCRG in a tracked vehicle final drive with FEA. Recently, Sánchez et al. [9, 10] proposed a load distribution model based on the minimum elastic potential (MEP) criteria for the calculations of contact stress and tooth root stress for HCRG and helical gears. Subsequently, they again presented an enhanced model for the calculations of the meshing stiffness and the loading sharing ratio for HCRG and LCRG considering the hertzian deflections [11]. Ye and Tsai [12] employed a loaded tooth contact analysis (LTCA) method to explore the contact characteristics of HCRG with and without flank modification in consideration of tip corner contact and shaft misalignment.

The gear teeth under heavily loaded condition are prone to deflection, which will result in the increase in vibration and noise of the mechanical systems. Tooth profile modification is regarded as one of the most effective ways to reduce the dynamic loads and vibrations of gear systems. Most of the literature on profile modification has been focused on the LCRG, but fewer contributions deal with the HCRG. Lee et al. [13] investigated the effects of linear profile modification and applied loading on the dynamic load and tooth root stress of HCRG. Whereafter, they examined and compared both linear and parabolic tooth profile modification of HCRG under various loading conditions [14]. It has been found that parabolic profile modification prevails over linear profile modification for HCRG because of its lower sensitivity to manufacturing errors. Yildirim [15, 16] proposed a new type of double relief which can be viewed as a superposition of a short and a long relief combining the advantages of these two limiting profile modifications. The research revealed that the overall performance of such double relief is superior to that of conventional single slope relief. Wang and Howard [17], and Vexlex [18] further confirmed that double profile relief can improve the dynamic behavior of HCRG. Faggioni et al. [19] developed a Random-Simplex optimization algorithm in search of the optimal profile modification to reduce gear vibration, using the peak to peak of the STE or the vibration level as the objective functions.

Many researchers have devoted themselves to the dynamic characteristics of low contact ratio spur and helical gears, and a great many useful results have been gained, such as periodic solution, sub-harmonic resonance, super-harmonic resonance, periodic coexistence and chaos. There is a great amount of literature on gear dynamics and dynamic modeling of gear systems. Özgüven and Houser [20] first reviewed the linear dynamic models of geared systems comprehensively. Wang et al. [21] gave an overview of the nonlinear vibration of geared systems. Özgüven and Houser [22] used a single degree of freedom (SDOF) nonlinear model

for the dynamic analysis of a gear pair, including the effects of TVMS, damping, gear errors, profile modifications and backlash. Based on this research, Özgüven [23] developed a six degrees of freedom (DOFs) model for the dynamic analysis of a gear system including shaft and bearing dynamics, and studied the effect of lateral-torsional vibration coupling on the dynamics of gears. Kahraman and Singh [24–26] proposed a series of studies for the influence of several factors on the frequency responses of nonlinear geared system based on the 1DOF and 3 DOFs models, such as time-variant mesh stiffness, gear backlash, bearing clearances, and external/internal excitations. Their results have laid a solid foundation for the work of the subsequent researchers. Blankenship et al. [27, 28] examined analytically and experimentally the nonlinear dynamic behavior of a mechanical oscillator with periodical time-varying parameters and clearance. Theodosiades et al. [29, 30] applied the piecewise-linear technique and multi-scale method to determine periodic steady-state motions and their stability properties. Al-shyyab and Kahraman [31, 32] presented a nonlinear dynamic model of a typical multi-mesh gear train to investigate period-one, sub-harmonic and chaotic motions by using multi-term Harmonic Balance Method (HBM). Vaishya and Singh [33, 34] earlier developed a SDOF dynamic model considering sliding friction between the teeth in contact. Vexlex and Sainsot [35] pointed out the potentially significant contribution of tooth friction to translational vibrations of pinions and gears, especially in the case of HCRG. He et al. [36, 37] proposed a new multi-degree of freedom (MDOF) spur gear model including realistic time-varying stiffness and sliding friction, and emphatically analyzed the effect of sliding friction on the system dynamic responses. Huang et al. [38] conducted the effects of rough surfaces on the dynamic performances of HCRG, in which the STE is described by the fractal theory.

In conclusion, few studies have been done on the dynamic characteristics of HCRG, especially in nonlinear dynamics. Nevertheless, the modeling theories and analytical methods about LCRG can apply equally to HCRG. Based on this idea, a MDOF nonlinear dynamic model for HCRG is established including the TVMS, STE, gear backlash and bearing radial clearance. The TVMS for HCRG is calculated based on an improved energy model, which considers the misalignment of root circle and base circle, and the realistic transition curve. The bifurcation and chaotic characteristics of HCRG are studied systematically and comprehensively using the numerical integral method. The results can provide the theoretical support for the design and vibration control of HCRG.

The structure of this study is organized as follows: the nonlinear dynamic model and equations of motion of the system are presented in Sect. 2, where the TVMS of HCRG is given. In Sect. 3, the equations of motion of the system are solved by the numerical integral method, and then the bifurcation and chaotic characteristics under different control

parameters are examined. Finally, some brief conclusions are given in Sect. 4.

## 2 Nonlinear dynamic modeling of HCRG

The nonlinear dynamic model of HCRG with multiple clearances is shown in Fig. 1 [25]. The gear pair is modeled as two disks connected by mesh stiffness, mesh damping, backlash and transmission error along the line of action (LOA). The gears are supported by two flexible rolling element bearings. Neglecting the effects of the friction between the teeth, only the lateral vibrations in the LOA direction and the torsional vibrations of two gears are considered. In this model,  $T_i$  ( $i = 1$ : pinion; 2: gear) are the constant external torques applied on pinion and gear, respectively;  $m_i$ ,  $I_i$  and  $R_i$  indicate the masses, moments of inertial and base radiuses of two gears, respectively;  $F_{bi}$  are the bearing radial preloads;  $k_{bi}$  and  $c_{bi}$  are the equivalent bearing stiffness and damping;  $k_m$  is the mesh stiffness of gear pair;  $c_m$  is the gear mesh damping;  $2b_n$  is the gear backlash;  $b_1$  and  $b_2$  are half the bearing radial clearances;  $e(t)$  represents the STE; The essential motions of the system can be described by four degrees of freedom, namely, two torsional motions  $\theta_1$  and  $\theta_2$ , and tow translational motions  $y_1$  and  $y_2$ .

### 2.1 Equations of motion of the system

According to Newtonian laws of motion, the system differential equations of motion can be expressed as follows:

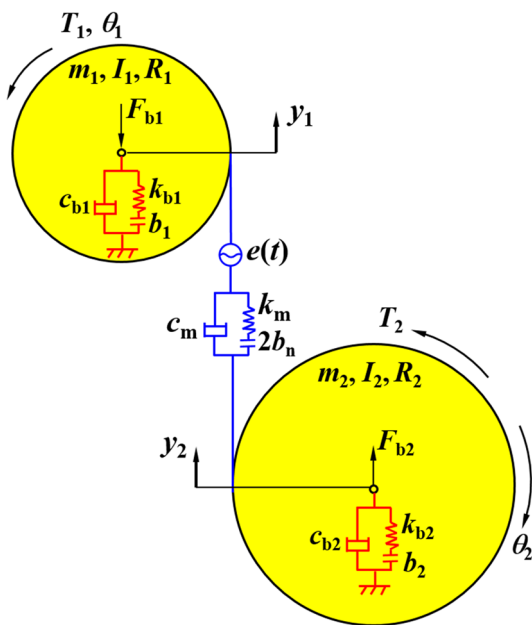


Fig. 1 Nonlinear dynamic model with multiple clearances

$$\begin{cases} m_1\ddot{y}_1 + c_{b1}\dot{y}_1 + k_{b1}f_{b1}(y_1) + c_m\dot{\delta} + k_m f_m(\delta) = -F_{b1} \\ m_2\ddot{y}_2 + c_{b2}\dot{y}_2 + k_{b2}f_{b2}(y_2) - c_m\dot{\delta} - k_m f_m(\delta) = F_{b2} \\ I_1\ddot{\theta}_1 + R_1c_m\dot{\delta} + R_1k_m f_m(\delta) = T_1 \\ I_2\ddot{\theta}_2 + R_2c_m\dot{\delta} + R_2k_m f_m(\delta) = -T_2 \end{cases} \quad (1)$$

where  $\delta$  is called the relative displacement between pinion and gear along the LOA, which is defined as the difference between the dynamic transmission error (DTE) and the STE  $e(t)$ .

$$\delta = R_1\theta_1 - R_2\theta_2 + y_1 - y_2 - e(t) \quad (2)$$

The STE  $e(t)$  is a kind of displacement excitation due to gear manufacturing error, which is usually indicated by first-order harmonic function.

$$e(t) = e_0 + e_a \sin(\omega_m t + \varphi) \quad (3)$$

where  $e_0$  is the mean value,  $e_a$  indicates the fluctuation amplitude,  $\varphi$  represents the initial phase, and  $\omega_m$  is the meshing frequency of gear pair,  $\omega_m = \omega_1 z_1 = \omega_2 z_2$ .

$f_m(\delta)$  is the nonlinear displacement function of gear backlash, which can be expressed as:

$$f_m(\delta) = \begin{cases} \delta - b_n & (\delta > b_n) \\ 0 & (|\delta| \leq b_n) \\ \delta + b_n & (\delta < -b_n) \end{cases} \quad (4)$$

Similarly, the nonlinear displacement function of the bearing radial clearance  $f_{bi}(y_i)$ , which can be written as follows:

$$f_{bi}(y_i) = \begin{cases} y_i - b_i & (y_i > b_i) \\ 0 & (|y_i| \leq b_i) \\ y_i + b_i & (y_i < -b_i) \end{cases}, \quad i = 1, 2 \quad (5)$$

Equation (1) can be further simplified into the following three-DOF equations in terms of the variable  $\delta$ .

$$\begin{cases} m_1\ddot{y}_1 + c_{b1}\dot{y}_1 + k_{b1}f_{b1}(y_1) + c_m\dot{\delta} + k_m f_m(\delta) = -F_{b1} \\ m_2\ddot{y}_2 + c_{b2}\dot{y}_2 + k_{b2}f_{b2}(y_2) - c_m\dot{\delta} - k_m f_m(\delta) = F_{b2} \\ m_e(\ddot{\delta} - \ddot{y}_1 + \ddot{y}_2) + c_m\dot{\delta} + k_m f_m(\delta) = F_m - m_e\ddot{e}(t) \end{cases} \quad (6)$$

where  $m_e$  is the equivalent mass of gear pair,  $m_e = I_1 I_2 / (I_1 R_2^2 + I_2 R_1^2)$ ;  $F_m$  is the average force transmitted by the gear pair,  $F_m = T_1 / R_1 = T_2 / R_2$ ;  $c_m = 2m\sqrt{k_0 \cdot m_e}$ ,  $k_0$  is the average mesh stiffness and  $m$  is the mesh damping ratio.

For the convenience of analysis, the differential equations (6) should be dimensionless. Introducing nominal dimension  $b_c$  and dimensionless time  $\tau = \omega_n t$ , where  $\omega_n = \sqrt{k_0 / m_e}$  is the natural frequency of gear pair, the

dimensionless displacement, velocity and acceleration can be expressed as, respectively.

$$\begin{aligned} \delta &= ub_c, \quad \dot{\delta} = \dot{u}\omega_n b_c, \quad \ddot{\delta} = \ddot{u}\omega_n^2 b_c, \quad y_i = \bar{y}_i b_c, \\ \dot{y}_i &= \dot{\bar{y}}_i \omega_n b_c, \quad \ddot{y}_i = \ddot{\bar{y}}_i \omega_n^2 b_c, \quad (i = 1, 2) \end{aligned} \tag{7}$$

Substituting Eqs. (7) into (6) yields the following dimensionless equations expressed in matrix form.

$$\begin{aligned} \begin{bmatrix} 1 & 0 & 0 \\ 0 & 1 & 0 \\ -1 & 1 & 1 \end{bmatrix} \begin{Bmatrix} \ddot{\bar{y}}_1 \\ \ddot{\bar{y}}_2 \\ \ddot{u} \end{Bmatrix} + 2 \begin{bmatrix} \zeta_{11} & 0 & \zeta_{13} \\ 0 & \zeta_{22} & -\zeta_{23} \\ 0 & 0 & \zeta_{33} \end{bmatrix} \begin{Bmatrix} \dot{\bar{y}}_1 \\ \dot{\bar{y}}_2 \\ \dot{u} \end{Bmatrix} \\ + \begin{bmatrix} k_{11} & 0 & k_{13} \\ 0 & k_{22} & -k_{23} \\ 0 & 0 & k_{33} \end{bmatrix} \begin{Bmatrix} \bar{f}_{b1}(\bar{y}_1) \\ \bar{f}_{b2}(\bar{y}_2) \\ f_m(u) \end{Bmatrix} = \begin{Bmatrix} -\bar{F}_{b1} \\ \bar{F}_{b2} \\ \bar{F}_m + \bar{F}_{eh} \end{Bmatrix} \end{aligned} \tag{8}$$

where  $\zeta_{ii} = c_{bi}/(2m_i\omega_n)$ ,  $\zeta_{i3} = c_m/(2m_i\omega_n)$  ( $i = 1, 2$ ),  $\zeta_{33} = c_m/(2m_e\omega_n)$ ,  $k_{ii} = k_{bi}/(m_i\omega_n^2)$ ,  $k_{i3} = k_m/(m_i\omega_n^2)$  ( $i = 1, 2$ ),  $k_{33} = k_m/(m_e\omega_n^2)$ ,  $\bar{F}_m = F_m/(m_e\omega_n^2 b_c)$ ,  $\bar{F}_{bi} = F_{bi}/(m_i\omega_n^2 b_c)$  ( $i = 1, 2$ ),  $\bar{F}_{eh} = F_e\Omega^2 \sin(\Omega\tau)$ ,  $F_e = e_a/b_c$ ,  $\Omega = \omega_m/\omega_n$ .

The dimensionless nonlinear displacement functions for backlash and bearing radial clearance are re-written as, respectively.

$$f_m(u) = \begin{cases} u - b & (u > +b) \\ 0 & (|u| \leq b) \\ u + b & (u < -b) \end{cases}; \quad b = b_n/b_c \tag{9}$$

$$\bar{f}_{bi}(\bar{y}_i) = \begin{cases} \bar{y}_i - \bar{b}_i & (\bar{y}_i > \bar{b}_i) \\ 0 & (|\bar{y}_i| \leq \bar{b}_i) \\ \bar{y}_i + \bar{b}_i & (\bar{y}_i < -\bar{b}_i) \end{cases}; \quad \bar{b}_i = b_i/b_c, \quad i = 1, 2 \tag{10}$$

### 2.2 Calculation of time-varying mesh stiffness

As is well known, TVMS changes periodically with the number of meshing teeth pair and the position of contact point. It is shown that TVMS is one of the main sources exciting the vibration of the gear system. There are many methods to calculate the TVMS, involving analytical method, finite element method (FEM), analytical-FE approach, and photo-elasticity technique. Considering the misalignment of gear root circle and base circle, and the accurate transition curve, Ma et al. [39] presented an improved mesh stiffness model, as shown in Fig. 2. Based the ANSYS software, Wang [7] developed an approach to predict the TVMS by establishing the contact elements. Wan et al. [40] also presented an improved TVMS algorithm by judging the relationship between the

teeth number and 42. Saxena et al. [41] proposed an analytical method to calculate the TVMS of the spur gear for different spall shapes, size and location considering sliding friction. Karma1 and Agarwal [42] calculated the mesh stiffness of high contact ratio spur gear and load sharing using the energy method. Raghuwanshi and Parey [43] measured the mesh stiffness of cracked spur gear using photo-elasticity technique. However, in these researches, the gear tooth is mostly modeled as a non-uniform cantilever beam on the base circle. In fact, the root circle and base circle are misaligned, which would affect the accuracy of TVMS.

To calculate the mesh stiffness conveniently and effectively, the improved potential energy method in [39] is adopted to calculate the TVMS of HCRG. Based on the elastic mechanics and beam theory, the bending stiffness  $k_b$ , shear stiffness  $k_s$  and axial compressive stiffness  $k_a$  can be obtained as follows:

$$\begin{aligned} \frac{1}{k_b} &= \int_{\frac{\pi}{2}}^{\alpha} \frac{[\cos\beta(y_\beta - y_1) - x_\beta \sin\beta]^2 dy_1}{EI_{y1}} d\gamma \\ &+ \int_{\tau_c}^{\beta} \frac{[\cos\beta(y_\beta - y_2) - x_\beta \sin\beta]^2 dy_2}{EI_{y2}} d\tau \end{aligned} \tag{11}$$

$$\frac{1}{k_s} = \int_{\frac{\pi}{2}}^{\alpha} \frac{1.2 \cos^2 \beta dy_1}{GA_{y1}} d\gamma + \int_{\tau_c}^{\beta} \frac{1.2 \cos^2 \beta dy_2}{GA_{y2}} d\tau \tag{12}$$

$$\frac{1}{k_a} = \int_{\frac{\pi}{2}}^{\alpha} \frac{\sin^2 \beta dy_1}{EA_{y1}} d\gamma + \int_{\tau_c}^{\beta} \frac{\sin^2 \beta dy_2}{EA_{y2}} d\tau \tag{13}$$

The Hertzian contact stiffness  $k_h$  and fillet-foundation stiffness  $k_f$  can be given by

$$\frac{1}{k_h} = \frac{4(1 - \nu^2)}{\pi EL} \tag{14}$$

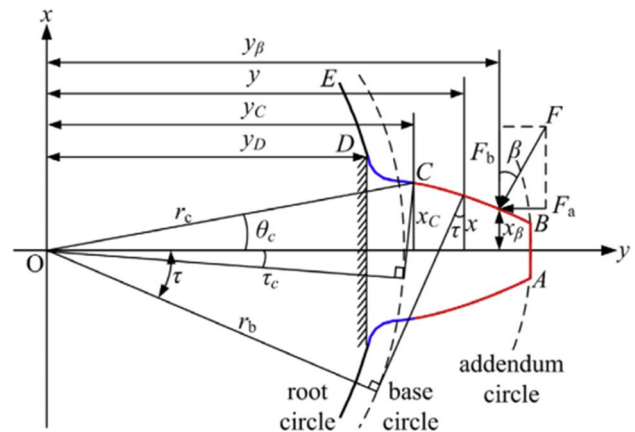


Fig. 2 Geometric model of the tooth profile [39]

$$\frac{1}{k_f} = \frac{\cos^2 \beta}{EL} \left\{ L^* \left( \frac{u_f}{S_f} \right)^2 + M^* \left( \frac{u_f}{S_f} \right) + P^* (1 + Q^* \tan^2 \beta) \right\} \tag{15}$$

Note that the detailed definitions of the symbols in Eqs. (11–15) can be found in Refs. [39, 44].

When a gear pair are meshing, the total potential energy  $U$  stored in a meshing tooth pair is the summation of Hertzian energy  $U_h$ , bending energy  $U_b$ , shear energy  $U_s$ , axial compressive energy  $U_a$  and fillet-foundation deformation energy  $U_f$  of each tooth, which can be expressed as:

$$U = \frac{F^2}{2k_s} = U_h + U_{b1} + U_{s1} + U_{a1} + U_{f1} + U_{b2} + U_{s2} + U_{a2} + U_{f2}$$

$$= \frac{F^2}{2} \left( \frac{1}{k_h} + \frac{1}{k_{b1}} + \frac{1}{k_{s1}} + \frac{1}{k_{a1}} + \frac{1}{k_{f1}} + \frac{1}{k_{b2}} + \frac{1}{k_{s2}} + \frac{1}{k_{a2}} + \frac{1}{k_{f2}} \right) \tag{16}$$

where  $k_s$  represents the total mesh stiffness of a pair of contact teeth, subscripts 1 and 2 represent pinion and gear, respectively.

Accordingly, the single-tooth-pair mesh stiffness can be give as:

$$k_s = 1 / \left( \frac{1}{k_h} + \frac{1}{k_{b1}} + \frac{1}{k_{s1}} + \frac{1}{k_{a1}} + \frac{1}{k_{f1}} + \frac{1}{k_{b2}} + \frac{1}{k_{s2}} + \frac{1}{k_{a2}} + \frac{1}{k_{f2}} \right) \tag{17}$$

For multiple tooth pairs, the total mesh stiffness is parallel combination of the mesh stiffnesses of all tooth pairs in contact, which can be written as:

$$k_m(t) = \sum_{i=1}^N \left( \frac{1}{k_h} + \frac{1}{k_{b1,i}} + \frac{1}{k_{s1,i}} + \frac{1}{k_{a1,i}} + \frac{1}{k_{f1,i}} + \frac{1}{k_{b2,i}} + \frac{1}{k_{s2,i}} + \frac{1}{k_{a2,i}} + \frac{1}{k_{f2,i}} \right)^{-1} \tag{18}$$

where  $N$  indicates the number of meshing tooth pair at the same time,  $N=2$  or  $3$  for HCRG.

**Table 1** Basic parameters of HCRG

Parameter/property	Pinion	Gear
Number of teeth	29	31
Module (mm)		3.0
Pressure angle (°)		20
Addendum coefficient		1.3
Face width (mm)		25
Center distance (mm)		89.7
Contact ratio		2.10
Mass (kg)	1.031	1.212
Modification coefficient ( $x_1/x_2$ )	-0.1	0
Moment of inertia (kg mm <sup>2</sup> )	1053	1416
Hub bore radius (mm)	25	25

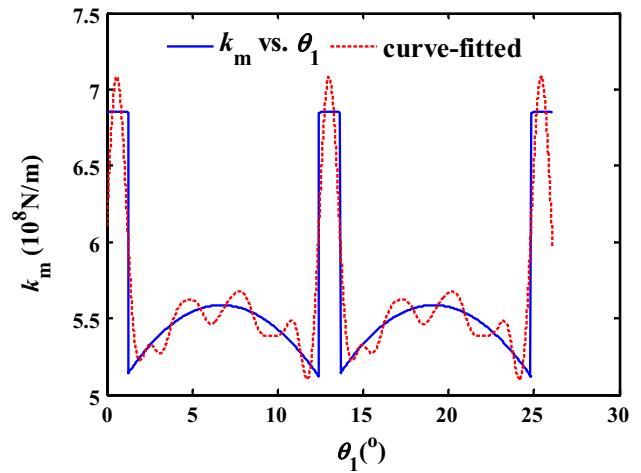


**Fig. 3** Fitting curve of TVMS of HCRG

The basic parameters of HCRG for this study are listed in Table 1. Based on the improved potential energy method, the TVMS of HCRG throughout a whole meshing period can be obtain. For the convenience of calculation, the TVMS is expanded into an eighth-order Fourier series form about  $\theta_1$  (°) (see Fig. 3).

$$k_m(\theta_1) = k_0 + \sum_{j=1}^8 [k_{aj} \cos(j\omega_\theta \theta_1) + k_{bj} \sin(j\omega_\theta \theta_1)] \tag{19}$$

where  $k_0$  is the average value of stiffness;  $k_{aj}$  and  $k_{bj}$  are

the coefficients of harmonic terms, as listed in Table 2.  $\omega_\theta = 2\pi z_1 / 360$ ,  $z_1$  is the tooth number of pinion.

By changing the coordinate, the TVMS  $k_m(\theta_1)$  can be converted into another form about time  $t$  to facilitate the subsequent calculation.

**Table 2** Coefficients of harmonic terms of mesh stiffness (N/m)

Harmonic term	$k_{aj}$	$k_{bj}$
1	1.391e7	5.061e6
2	2.506e7	1.65e7
3	1.935e7	2.255e7
4	1.089e7	2.393e7
5	3.084e6	2.127e7
6	-2.221e6	1.589e7
7	-4.255e6	9.514e6
8	-3.228e6	3.858e6
$k_0$	5.589e8	

$$k_m(t) = k_0 + \sum_{j=1}^8 [k_{aj} \cos(j\omega_m t) + k_{bj} \sin(j\omega_m t)] \quad (20)$$

where  $\omega_m$  is the above-mentioned meshing frequency of gear pair.

### 3 Numerical simulation and discussion

Due to the existence of time-varying stiffness, gear backlash, and bearing radial clearance, the gear system is a complex system with strong nonlinearity and time variation. In order to understand comprehensively the dynamic features of HCRG, excitation frequency  $\Omega$ , mesh damping ratio  $\xi_m$ , gear backlash  $b$ , error fluctuation  $F_e$ , and bearing radial clearances  $\bar{b}_1, \bar{b}_2$  are selected as bifurcation parameters to study the influence on the system responses. The system equations of motion are solved by the 4th–5th order Runge–Kutta numerical integration method, and its nonlinear dynamic characteristics are systematically analyzed through the bifurcation diagrams, LLE charts, time-domain waveforms, FFT spectra, Poincaré maps and phase diagrams. The main geometric parameters of HCRG are seen in Table 1, and the invariant parameters of this simulation are listed as follows: input power  $P = 200$  kW, nominal dimension  $b_c = 10 \mu\text{m}$ , equivalent bearing stiffness  $k_{b1} = k_{b2} = 3.5\text{e}8$  N/m, bearing damping  $c_{b1} = 1.90\text{e}3$  N s/m,  $c_{b2} = 2.06\text{e}3$  N s/m; the initial values of control parameters are set as: error fluctuation  $e_a = 5 \mu\text{m}$ , gear backlash  $b_n = 40 \mu\text{m}$ , bearing radial clearances  $b_i = 10 \mu\text{m}$ , and mesh damping ratio  $\zeta_m = 0.04$ .

#### 3.1 Effects of excitation frequency $\Omega$

Excitation frequency  $\Omega$  reflects the rotational speed of pinion or gear, and is one of the key parameters that affect the

dynamic behaviors of the mechanical transmission system. Figure 4a presents the bifurcation diagram of the relative torsional displacement  $u$  with the change of excitation frequency  $\Omega$ . The corresponding LLE chart is shown in Fig. 4b. It can be seen from the bifurcation diagram and the LLE chart in Fig. 4 that there exist kinds of motion forms within the different ranges of values of the excitation frequency, such as period-1, period-2, multi-period, and chaotic motions. When  $\Omega \in [0.2, 1.046]$ , the system is in period-1 motion state and the LLEs are negative values. In the frequency range of  $\Omega \in [1.047, 1.282]$ , the system undergoes a series of transitions among quasi-periodic, multi-period and chaotic motions and there appears zero, positive and negative values in the LLE chart, which will be subsequently discussed in detail. When  $\Omega \in [1.283, 1.685]$ , the system response changes from period-1 motion to period-2 motion and the corresponding LLEs show negative. When  $\Omega \in [1.686, 2.32]$ , the system enters into chaotic region by crisis way, when the LLEs hold positive. Eventually, the system response converges to period-1 motion by inverse period-doubling bifurcation and the corresponding LLEs change from positive to negative. Moreover, the phenomenon of frequency hopping occurs at the point of  $\Omega = 0.906$ , where the LLE is  $-0.008686$ .

Figure 5 shows the partial enlarged view and the corresponding LLE chart at the range of  $\Omega \in [1.0, 1.3]$ . It is quite clear that the system exhibits complex nonlinear behaviors. In order to reveal the evolution process of the system responses more clearly, the phase diagrams and Poincaré maps under different excitation frequencies are listed in Fig. 6. When  $\Omega$  is less than 1.047, the system is in period-1 motion state and the corresponding LLEs show negative, as seen in Figs. 6a and 5b. As  $\Omega$  is increased to 1.055, the system turns into quasi-periodic motion from period-1 motion by Hopf bifurcation. As displayed in Fig. 6b, the phase diagram shows a closed curve band with a certain thickness

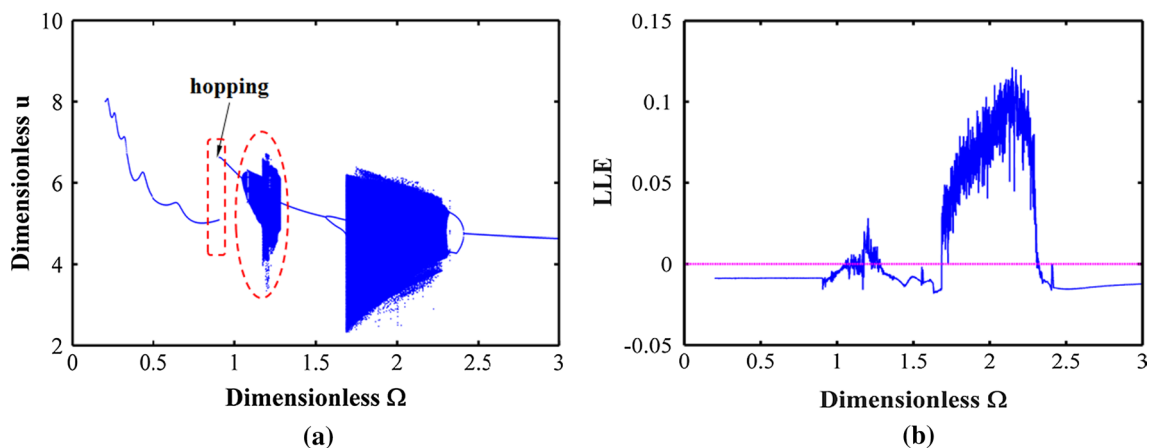
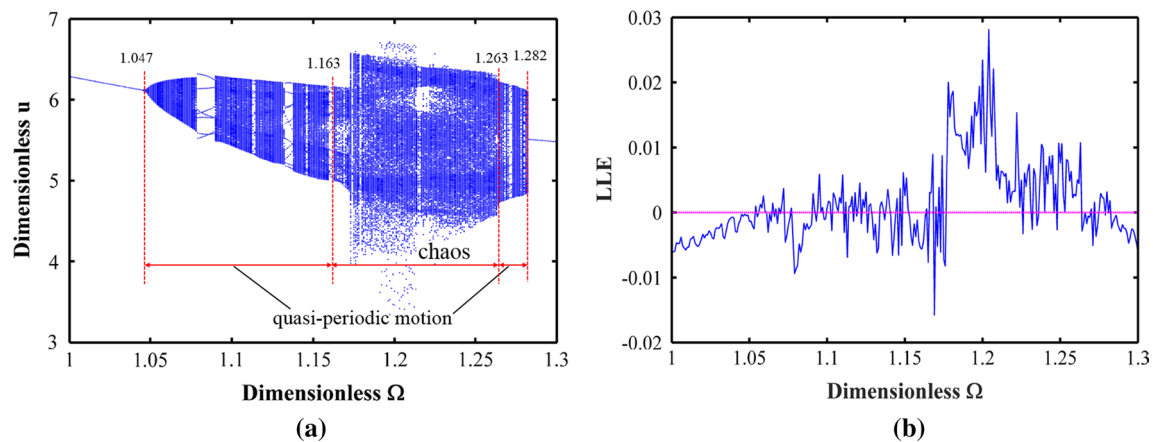


Fig. 4 Bifurcation diagram and largest Lyapunov exponent chart with the change of  $\Omega$



**Fig. 5** Partial enlarged view and largest Lyapunov exponent at the range of  $\Omega \in [1.0, 1.3]$

and Poincaré map is a closed smooth curve. Besides, the LLE is equal to zero in Fig. 5b. All these characteristics reveal that the system is in quasi-periodic motion state. As  $\Omega$  is further increased, the thickness of phase diagram gradually becomes larger and the Poincaré maps show some twisted-closed curves, which mean that chaotic motion is about to occur, as can be observed from Fig. 6d, f, h, where the LLEs are 0. When  $\Omega$  increases to 1.163, the system enters into chaotic region until  $\Omega$  value is equal to 1.263, as can be identified from Fig. 6j, k, where the LLEs are 0.00391 and 0.01079. As  $\Omega$  is changed from 1.264 to 1.282, it can be inferred from Fig. 6l, n that the system returns to quasi-periodic motion, where the LLEs are 0. Finally, the system leaves quasi-periodic motion, and then comes into period-1 motion by crisis way, as shown in Fig. 6o. In addition, from Fig. 6c, e, g, i, m, there also exist several transient multi-period motion windows between these quasi-periodic regions, which are period-7, period-18, period-11, period-15 and period-19 motions. The corresponding LLEs are  $-0.001638$ ,  $-0.006928$ ,  $-0.002968$ ,  $-0.005638$  and  $-0.005116$ , respectively.

From the above analysis, when the excitation frequency of the system is in the intervals of  $\Omega \in [0.2, 1.046]$ ,  $[1.283, 1.685]$  and  $[2.32, 3.0]$ , the HCRG manifests as simple period-1 or period-2 motions, which are the better working areas of the system. This will contribute to improve the system stability, reduce the vibration and avoid the chaos.

### 3.2 Effects of gear backlash $b$

Considering these factors like gear lubrication, tooth elastic deformation, thermal expansion and so on, a certain amount of gear backlash must be reserved between the non-working tooth profiles. However, the existence of gear backlash can result in the teeth separation and impact. Thus, it is vital

to explore the effects of gear backlash on the dynamic behaviors of the system and to select a proper gear backlash. Here, gear backlash  $b$  is used as a control parameter and the remaining parameters are kept unchanged. Excitation frequency is taken as  $\Omega = 1.08, 1.283, 1.685, 1.70$ . The bifurcation diagrams of the system with the change of gear backlash are shown in Fig. 7.

It can be seen from Fig. 7 that, when the remaining parameters are invariant and the excitation frequency takes different values, the system behaves as some simple periodic properties under smaller gear backlashes, e.g., period-1 and period-2 motions, which are favor of the system stability. With the increase in gear backlash  $b$ , the bifurcation features of the system obviously change. For example, when  $\Omega = 1.283$ , as shown in Fig. 7b, the system goes through the following switching process: period-1 motion  $\rightarrow$  quasi-periodic motion  $\rightarrow$  period-8 motion  $\rightarrow$  period-4 motion  $\rightarrow$  transient quasi-periodic motion  $\rightarrow$  period-1 motion, as can be identified by Figs. 8, 9, 10, 11, 12 and 13. As  $\Omega$  increases, the range of periodic motion of the system is gradually narrowing and that of chaotic motion is increasing in Fig. 7c, d, which are adverse to the system stability. The response analyses under the other excitation frequencies are similar to Fig. 7b, so they are not repeated here.

The above analysis shows that the HCRG keeps periodic motion under smaller gear backlash and the system runs smoothly. Therefore, in the design process of HCRG, while ensuring good lubrication of gears, a proper gear backlash should be selected, which is of great significance to reduce the vibration and noise of gear transmission system.

### 3.3 Effects of mesh damping ratio $\zeta_m$

To obtain the effects of mesh damping ratio  $\zeta_m$  on the system nonlinear dynamics and to adjust the system structure, mesh damping ratio  $\zeta_m$  is used as the analysis parameter and the

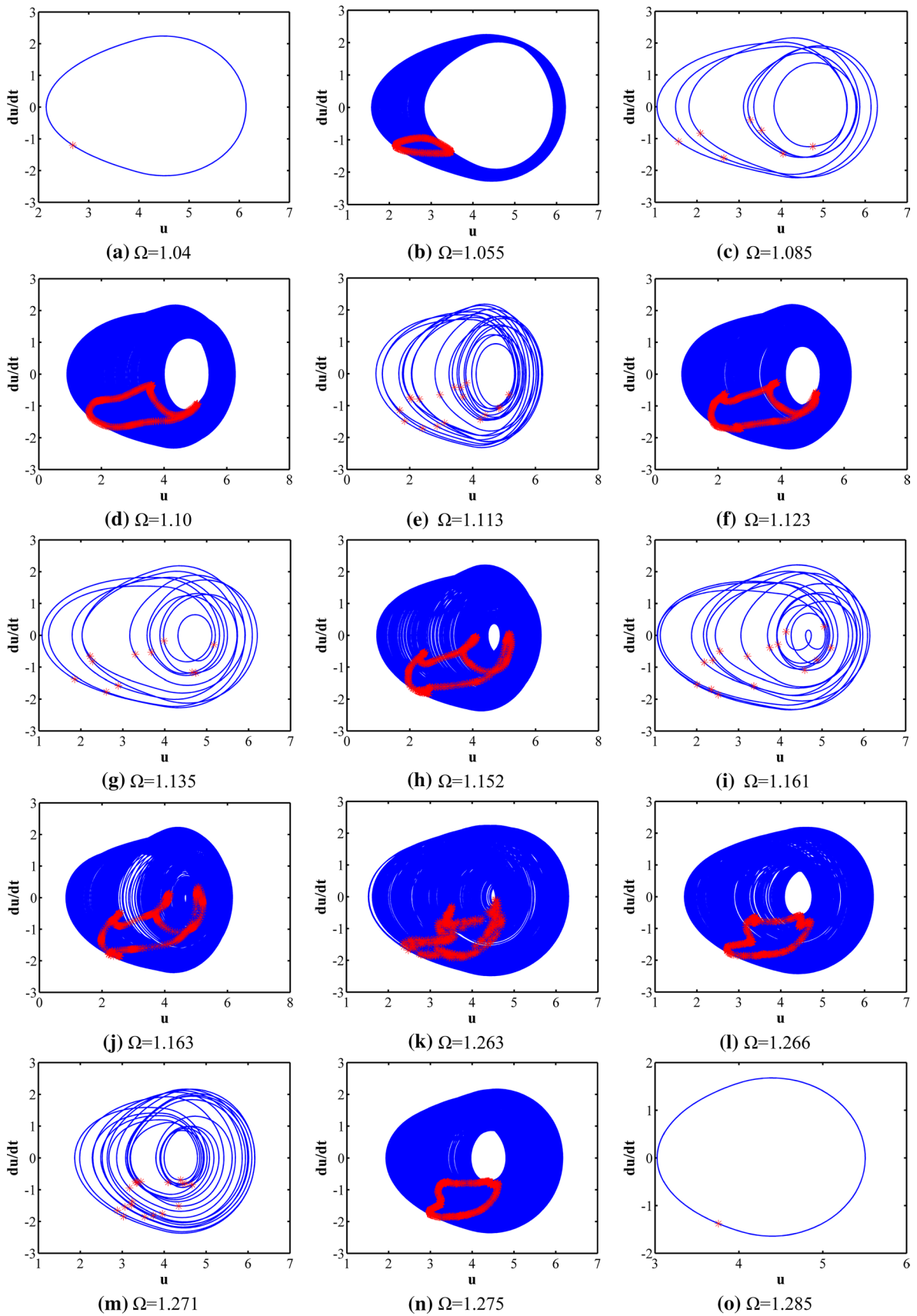


Fig. 6 Evolution process of the system responses at the range of  $\Omega \in [1.0, 1.3]$



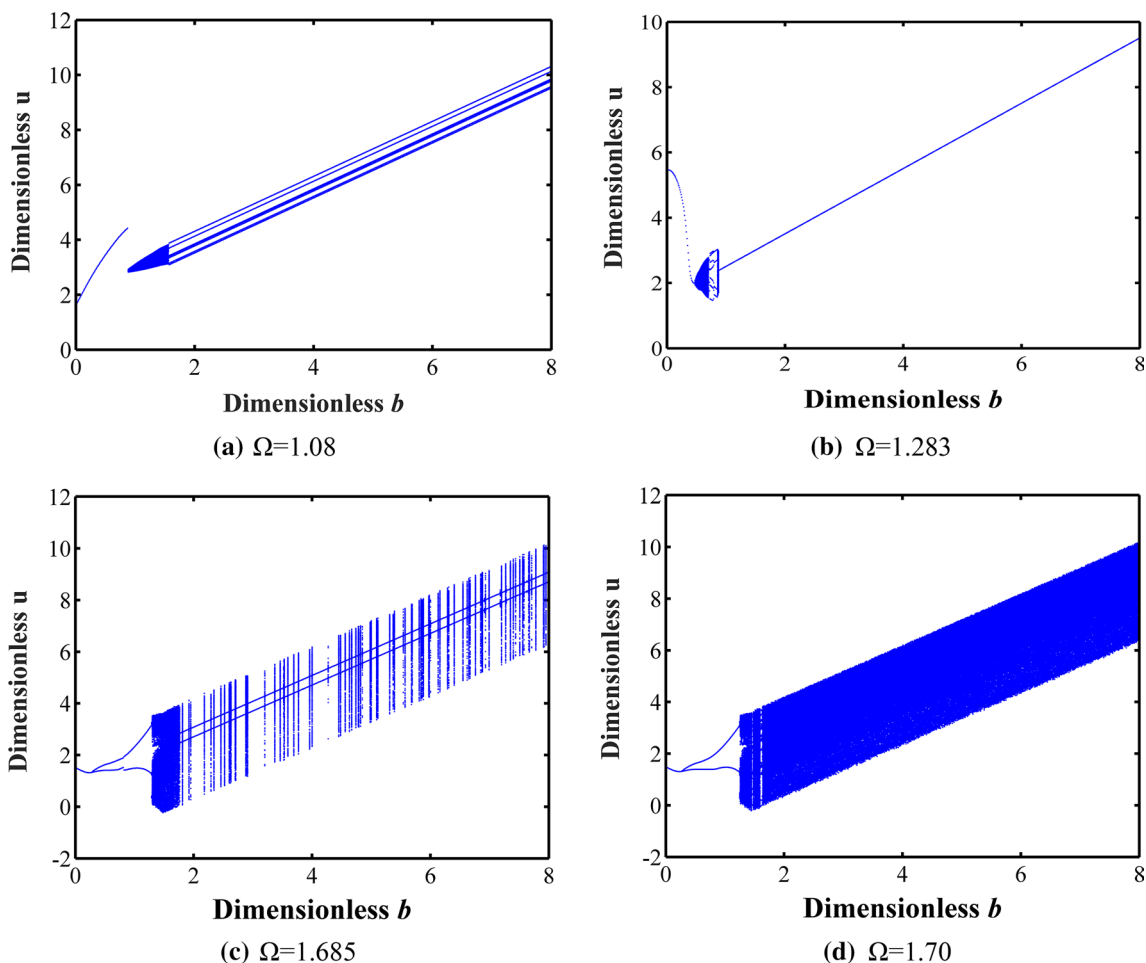


Fig. 7 Bifurcation diagrams with the change of  $b$  under different excitation frequencies

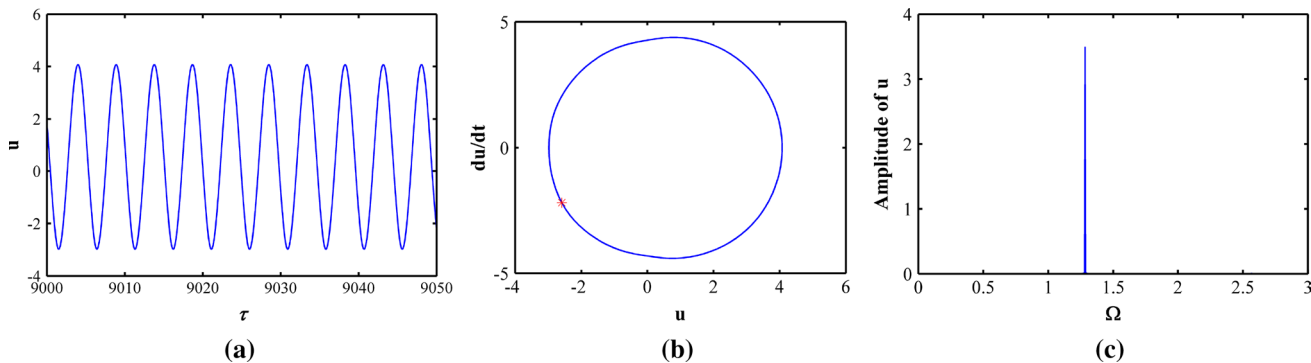
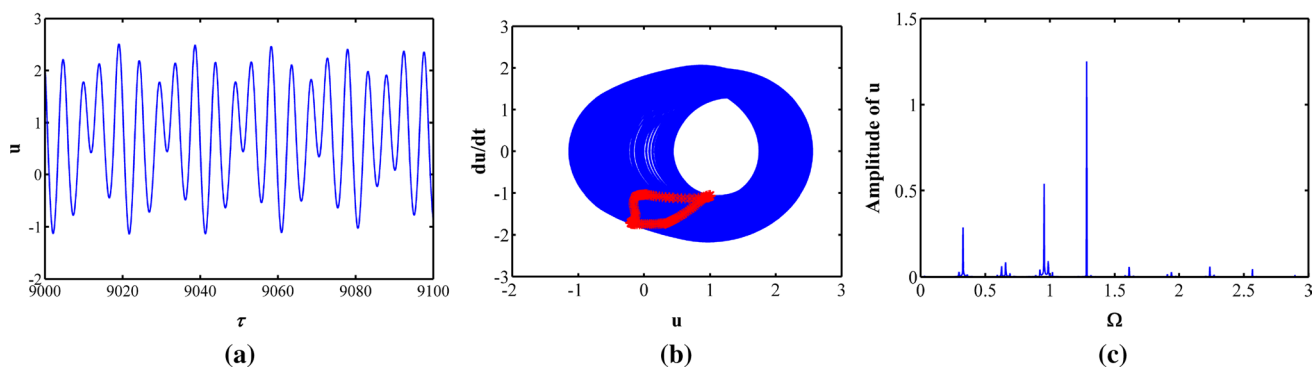


Fig. 8 Dynamic response curves at  $b=0.3$ . **a** Time-domain waveform, **b** phase diagram and Poincaré map and **c** FFT spectrum

other parameters are kept invariant. Excitation frequency is taken as  $\Omega = 1.08, 1.283, 1.685, 1.70$ . Figure 14 shows the bifurcation diagrams of the system with the change of  $\zeta_m$  in this range of  $\zeta_m \in [0.03, 0.17]$ .

It can be seen from the bifurcation diagrams in Fig. 14 that, when the remaining parameters are invariant and the excitation frequency takes various values, the system shows different bifurcation behaviors with the decrease of



**Fig. 9** Dynamic response curves at  $b=0.6$ . **a** Time-domain waveform, **b** phase diagram and Poincaré map and **c** FFT spectrum

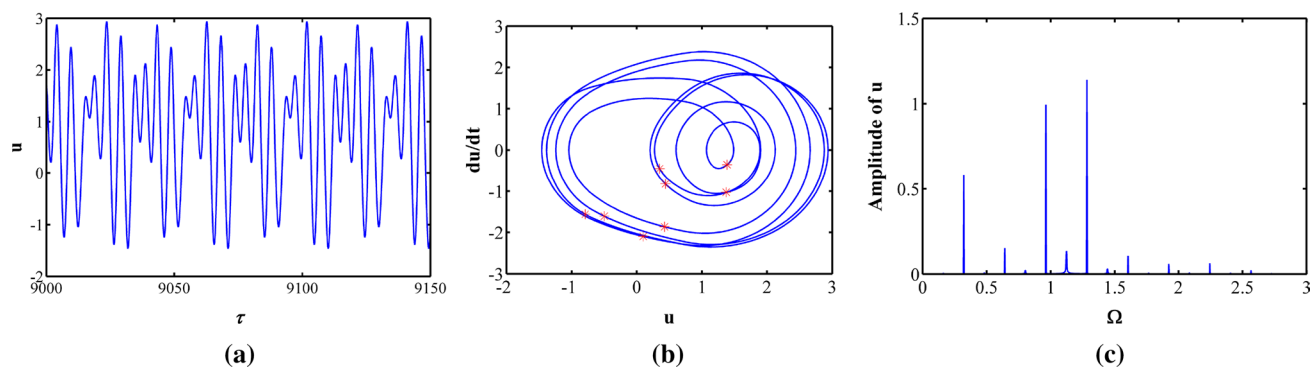


**Fig. 10** Dynamic response curves at  $b=0.75$ . **a** Time-domain waveform, **b** phase diagram and Poincaré map and **c** FFT spectrum

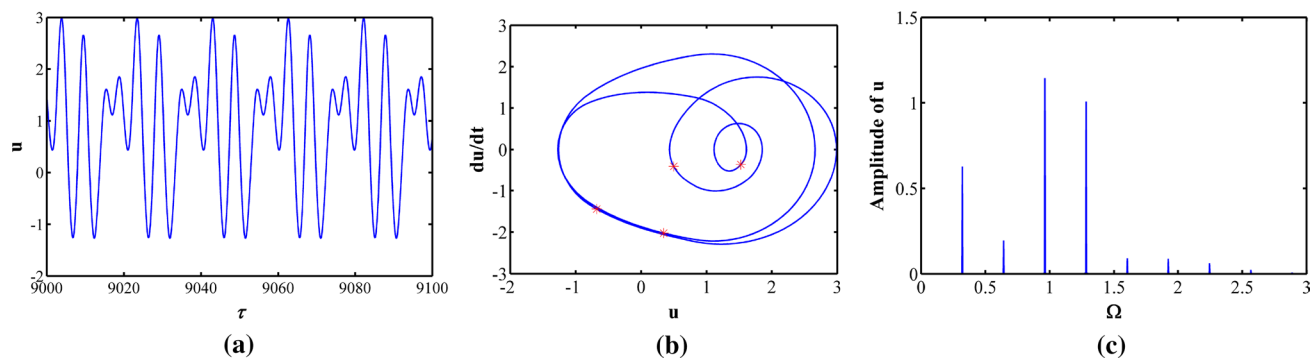


**Fig. 11** Dynamic response curves at  $b=0.82$ . **a** Time-domain waveform, **b** phase diagram and Poincaré map and **c** FFT spectrum

$\zeta_m$ . As shown in Fig. 14a, b, the system directly changes from period-1 motion to quasi-periodic motion by Hopf bifurcation. From Fig. 14c, d, the system first bifurcates into period-2 motion from period-1 motion and then enters into chaotic motion by crisis. For instance, when  $\Omega = 1.08$ , with the reduction of  $\zeta_m$ , the system first undergoes the transition from period-1 motion to quasi-periodic motion, then enters into period-7 motion region, and finally returns

to quasi-periodic motion, as can be identified from Fig. 15. From the overall bifurcation diagrams, the system eventually converges to period-1 motion under higher mesh damping ratio. Therefore, the higher mesh damping ratio will contribute to enhance the system stability and avoid the chaotic motion. The response analyses of the other bifurcation diagrams are similar, so they are not repeated here.

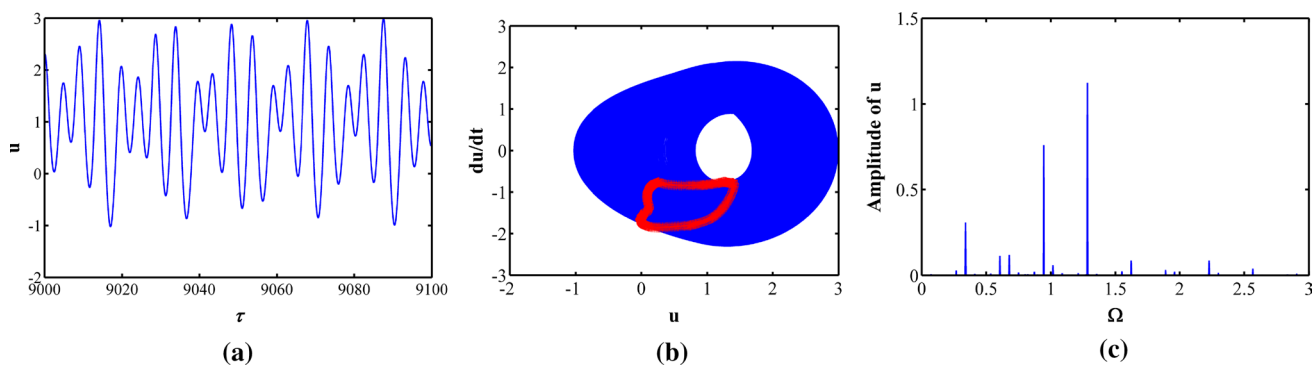


Fig. 12 Dynamic response curves at  $b=0.87$ . **a** Time-domain waveform, **b** phase diagram and Poincaré map and **c** FFT spectrum

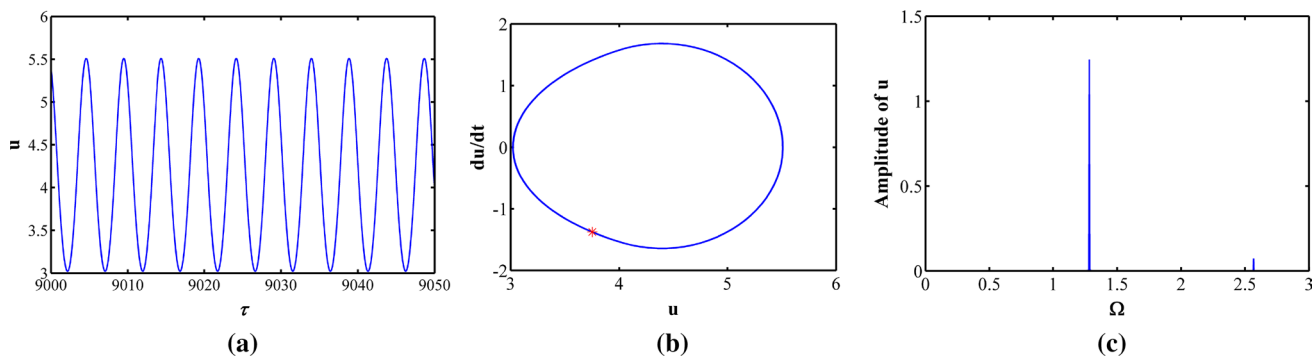
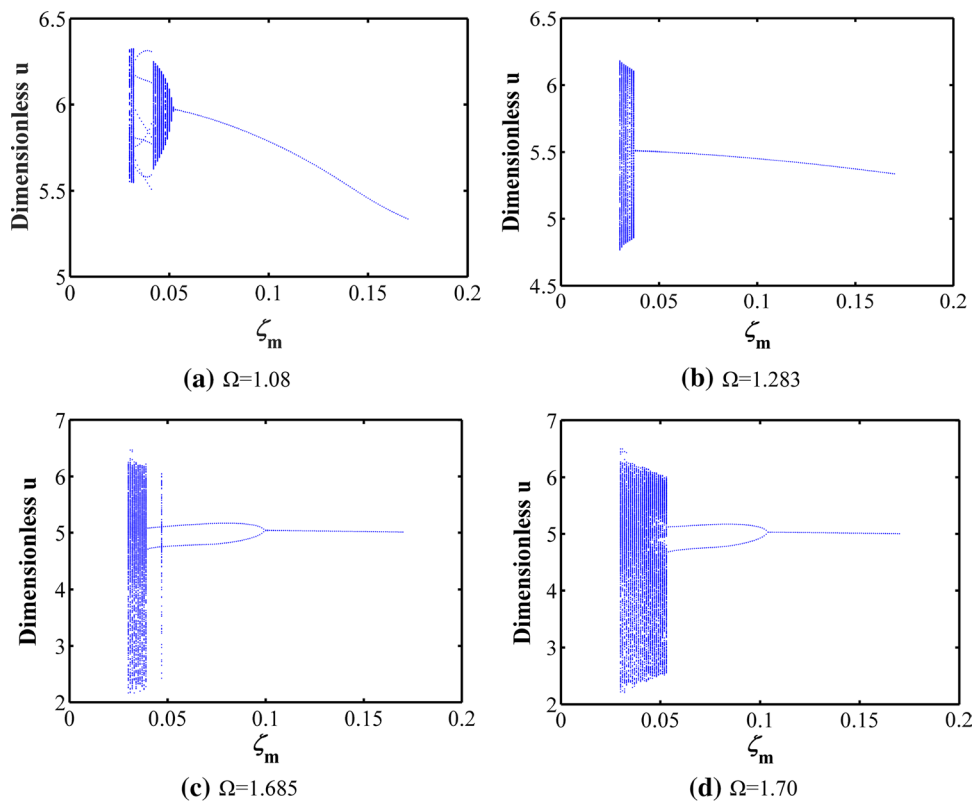
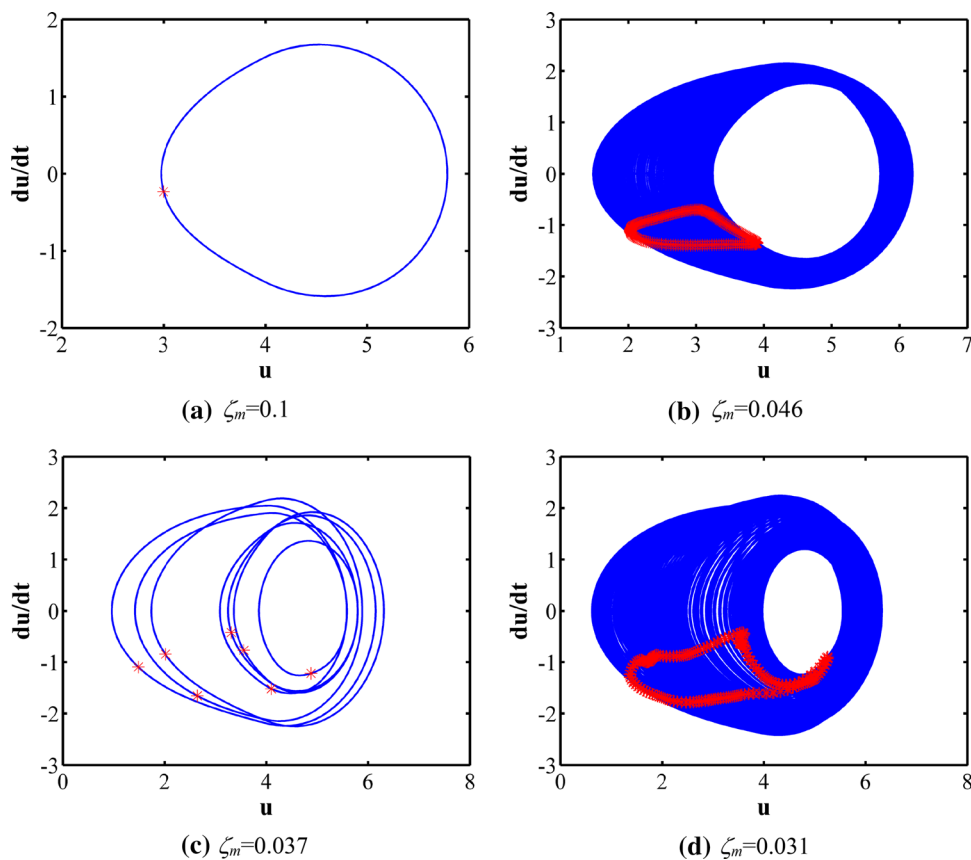


Fig. 13 Dynamic response curves at  $b=4.0$ . **a** Time-domain waveform, **b** phase diagram and Poincaré map and **c** FFT spectrum

Fig. 14 Bifurcation diagrams with the change of  $\zeta_m$  under different excitation frequencies



**Fig. 15** Evolution process of the system responses at  $\Omega=1.08$



### 3.4 Effects of error fluctuation $F_e$

Owing to multi-tooth meshing all the time, HCRG is very sensitive to tooth profile errors. Therefore, it is necessary to investigate the influence of error fluctuation on the nonlinear behavior of the system. Figure 16 presents the bifurcation diagrams of the system using error fluctuation  $F_e$  as a varying parameter under different excitation frequencies  $\Omega=1.5, 1.6, 1.7, 2.0$ . As can be seen from the bifurcation figures in Fig. 16, with the increase in error fluctuation, the system bifurcates into period-2 motion from period-1 motion and then suddenly enters into chaotic motion region. Furthermore, the region of the simple periodic motion is gradually decreasing with increasing the excitation frequency.

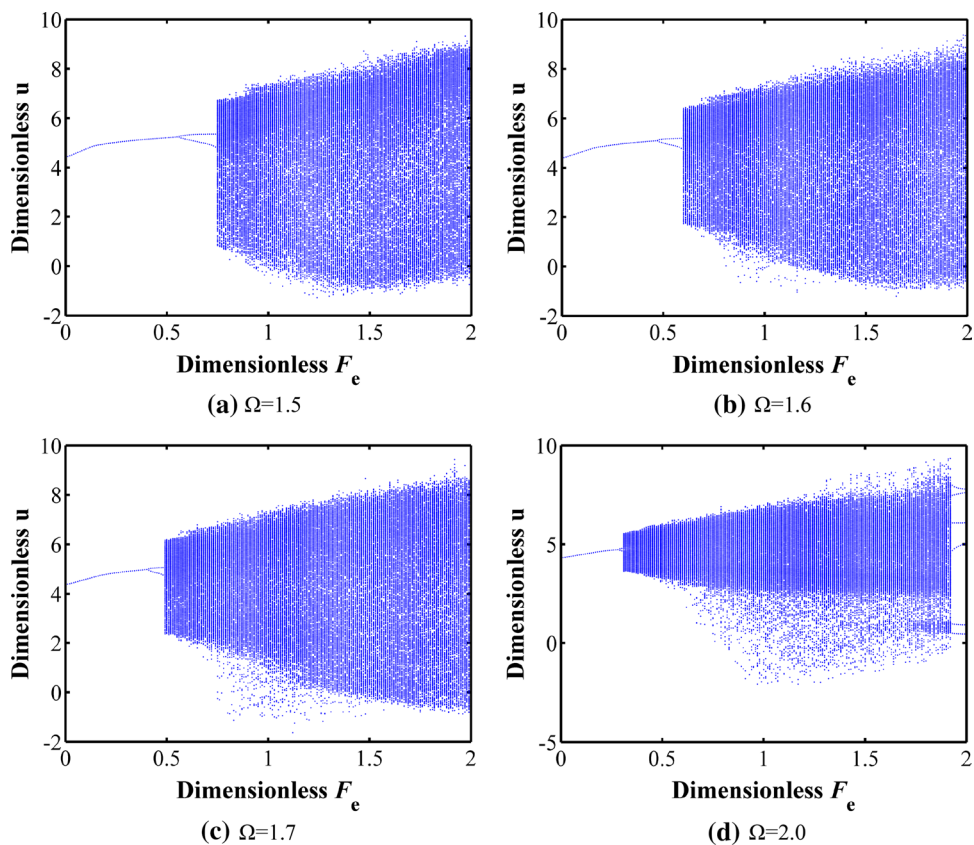
Meanwhile, Fig. 17 shows the changes of the system response with the excitation frequency under different error fluctuation values. It can be clearly seen from the bifurcation diagrams in Fig. 17 that the error fluctuation has a significant effects on the nonlinear behaviors of HCRG. When the error fluctuation  $F_e=0$ , namely, the gears have perfect involute profiles, the dynamic response curve is continuous and no bifurcation phenomenon occurs, as shown in Fig. 17a. As  $F_e$  is further increased, the system gradually presents complex nonlinear behaviors, involving jump discontinuity, quasi-periodic response, bifurcation, chaotic response, etc. The

nonlinear analysis for Fig. 17c has been done in Sect. 3.1. Comparing Fig. 17c with Fig. 17d, it can be found that, with the increase of  $F_e$ , the total range of chaotic window is gradually enlarging and the vibration amplitudes obviously increase, which are not good for the system stability. Figure 18 presents the amplitude-frequency spectra under four different error fluctuation values when  $\Omega=0.5$  (namely, the same rotating speed). It can be seen that the dimensionless amplitudes at the fundamental frequency positions  $\Omega=0.5$  are increasing with the increase of  $F_e$ . Accordingly, special attention should be paid to the manufacturing and processing of HCRG to attain the highest quality gears possible, so that the influence of tooth random errors can be minimized. The response analysis of the system about  $F_e=0.8$  is similar to that of  $F_e=0.5$ , so it is not repeated again here.

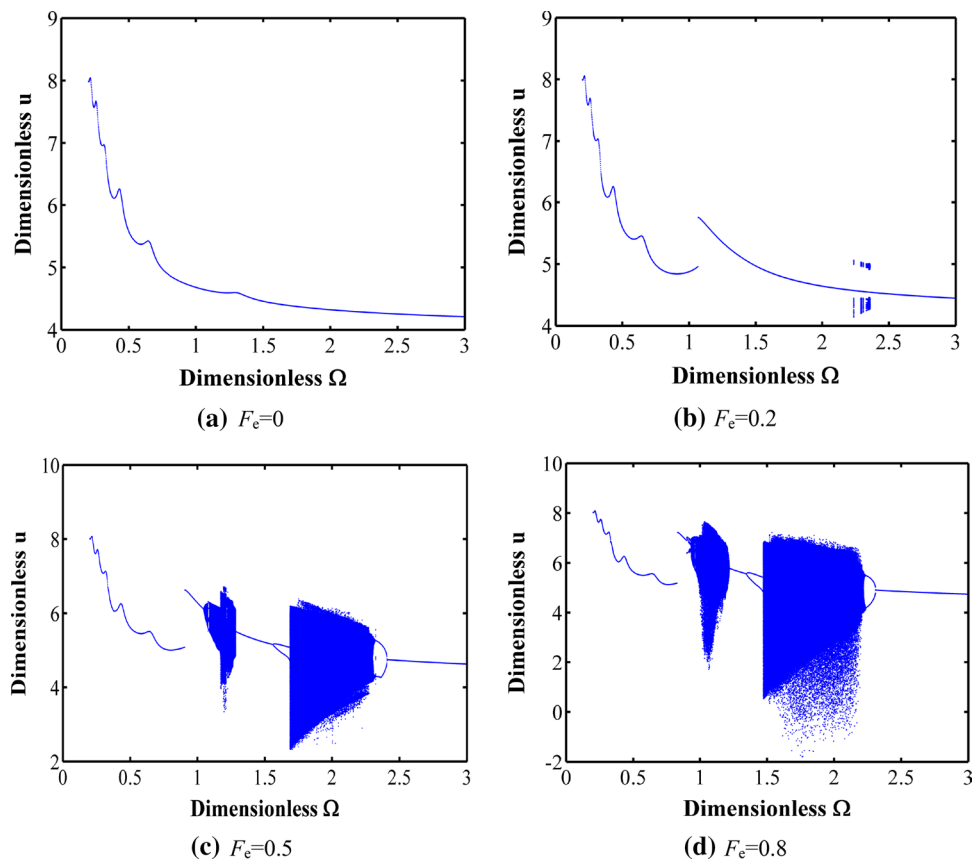
### 3.5 Effects of bearing radial clearance $\bar{b}_1, \bar{b}_2$

The bearing radial clearance is also one of the main factors that cause the nonlinear behaviors of the geared systems. Therefore, it is also very important to study the influence of bearing radial clearance on the system nonlinear dynamics and to select a suitable bearing clearance. Figure 19 shows the bifurcation diagrams of the system using the bearing radial clearance as a bifurcation parameter when  $\Omega$  takes

**Fig. 16** Bifurcation diagrams with the change of  $F_e$  under different excitation frequencies



**Fig. 17** Effects of error fluctuation on bifurcation and chaos characteristics



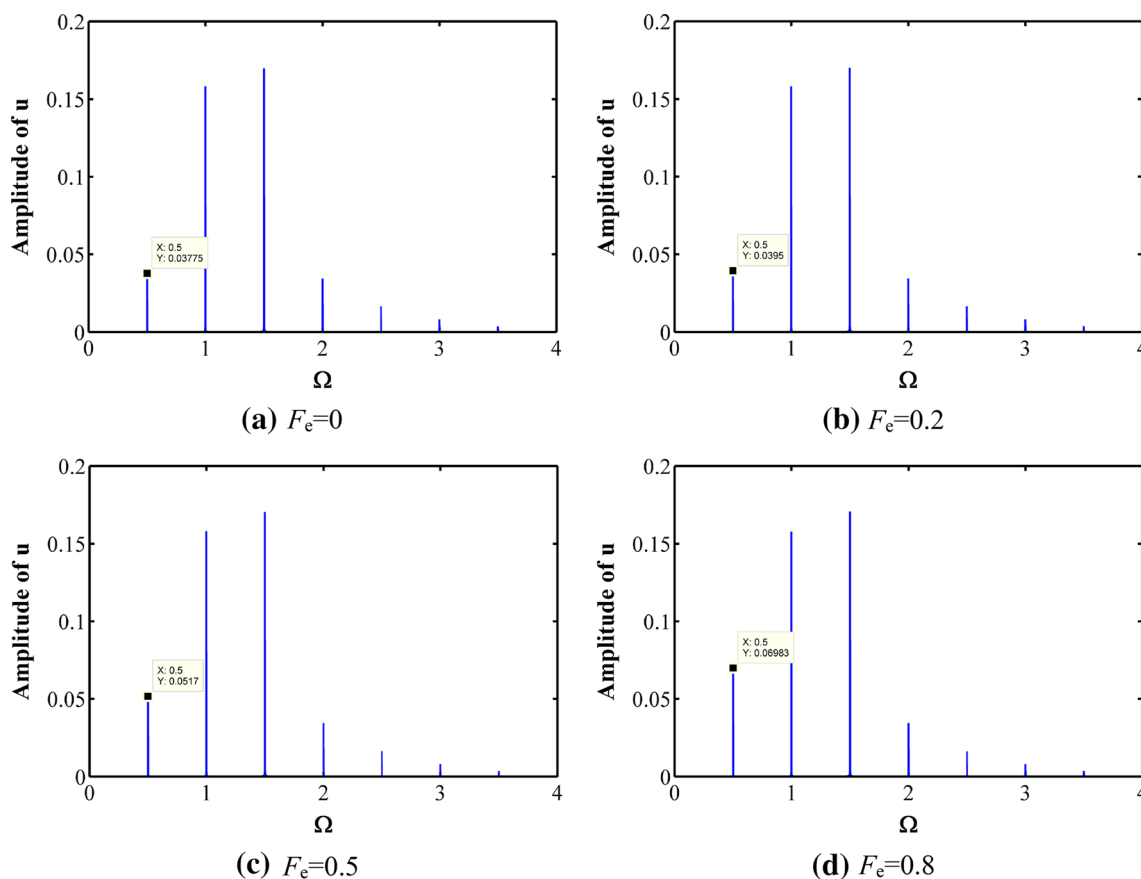


Fig. 18 Amplitude–frequency spectra at  $\Omega=0.5$

different values 0.906, 1.08, 1.283 and 1.685, and the other parameters remain invariant.

It can be clearly found from the bifurcation diagrams in Fig. 19 that the bearing radial clearance has a much weaker effect on the system nonlinear behavior when compared with gear backlash. When the bearing radial clearance is in the region of  $\bar{b}_1, \bar{b}_2 \in [0, 3]$ , the system is in a same motion state in most regions. When  $\Omega=0.906$ , the system is always in period-1 motion state, as shown in Fig. 19a. When  $\Omega=1.08$ , the system is in quasi-periodic state at a small scope of  $\bar{b}_1, \bar{b}_2 \in [0, 0.14]$ , and then enters a larger region with a stable period-7 motion, as can be seen from Fig. 19b. When  $\Omega=1.283$ , as illustrated in Fig. 19c, the system performs quasi-periodic motion at a very narrow range of  $\bar{b}_1, \bar{b}_2 \in [0, 0.03]$ , then rapidly comes into stable period-1 motion region. When  $\Omega=1.685$ , the system maintains stable period-2 motion all the time, though the bifurcation diagram shows some burrs, as displayed in Fig. 19d. The common phenomenon of the weak coupling effect about bearing radial clearance is further validated by different parameter combinations.

The above analysis shows that the bearing radial clearance only produce weak and ignorable coupling effects on the nonlinear features of the system. From the point of view of convenient modeling, the effect of nonlinearity of bearing radial clearance may be neglected in this study. However, to satisfy bearing lubrication and prevent the interference between raceway and rolling elements, the bearing radial clearance should be reasonably chosen according to the recommended scopes of the corresponding standard.

### 4 Conclusions

This paper establishes a nonlinear dynamic model for HCRG, which contains several nonlinear factors, such as TVMS, STE, gear backlash and bearing radial clearance. Based on the improved potential energy model, the TVMS of HCRG is calculated and then fitted into a Fourier series form. The system equations of motion are normalized and then solved using the 4th–5th order Runge–Kutta numerical integration method. The influence of excitation frequency,

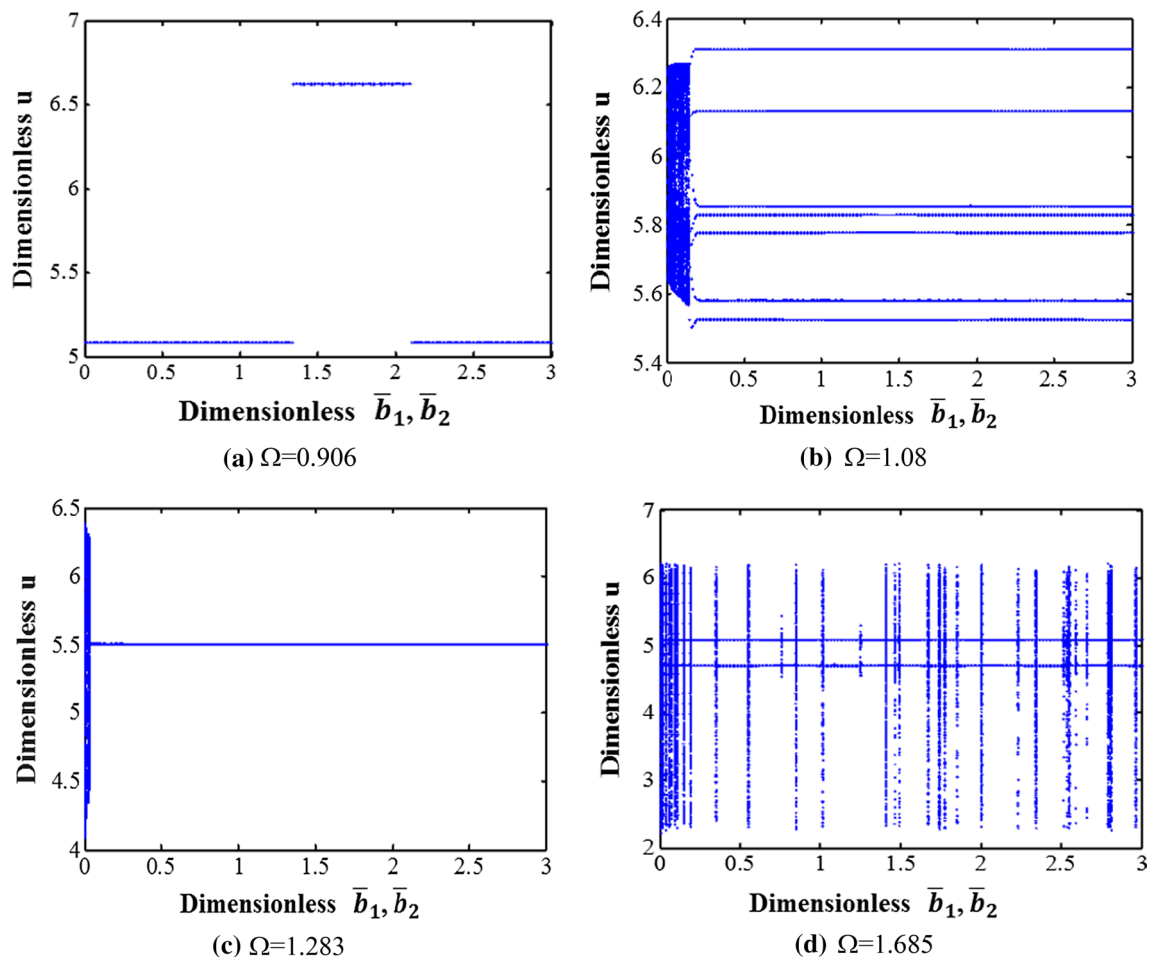


**Fig. 19** Bifurcation diagrams with the change of  $\bar{b}_1, \bar{b}_2$  under different excitation frequencies

gear backlash, mesh damping ratio, error fluctuation, and bearing radial clearance on the nonlinear dynamic characteristics of the system is comprehensively analyzed by the bifurcation diagrams, time-domain waveforms, FFT spectra, Poincaré maps, phase diagrams as well as LLE charts.

The main conclusions can be summarized as follows:

1. The HCRG exhibits rich bifurcation and chaotic characteristics under the influence of multiple factors. With the change of excitation frequency, the system shows complex motion states, including simple periodic, multi-periodic, quasi-periodic and chaotic motions and so on. It is found that there are three typical routes to chaos in the response, i.e., period-doubling bifurcation to chaos, quasi-period to chaos and crisis to chaos.
2. The smaller gear backlash and larger mesh damping ratio will contribute to improve the system stability and reduce the vibration and noise, which is of great significance for guiding the dynamic design of the HCRG.
3. The bearing radial clearance has a weaker influence on the system nonlinear behaviors and no bifurcation behavior could be observed under this bifurcation parameter.
4. The error fluctuation has significant effects on the nonlinear behaviors of the HCRG. With the increase in error fluctuation, the system responses become more and more complicated and the range of periodic motion decreases step by step, which goes against the system stability. Therefore, the HCRG with high degree of accuracy will help to avoid chaos and enhance the system stability.

**Acknowledgements** This work is supported by the National Natural Science Foundation of China (51775156), Natural Science Foundation of Anhui Province of China (1908085QE228) and the Fundamental Research Funds for the Central Universities of China (JZ2018H-GTA0206, JZ2018HGBZ0101, PA2019GDZC0101).

## References

- Cornell RW, Westervelt WW (1978) Dynamic tooth loads and stressing for high contact ratio spur gears. *J Mech Des* 100(1):69–76
- Rosen KM, Frint HK (1982) Design of high contact ratio gears. *J Am Helicopter Soc* 27(4):65–73
- Rameshkumar M, Sivakumar P, Sundares S et al (2010) Load sharing analysis of high-contact-ratio spur gears in military tracked vehicle applications. *Gear Technol* 1:43–50
- Staph HE (1976) A parametric analysis of high contact ratio spur gears. *ASLE Trans* 19(3):201–215
- Elkholy AH (1985) Tooth load sharing in high contact ratio spur gears. *J Mech Des* 107:11–16
- Tavakoli MS, Houser DR (1986) Optimum profile modifications for the minimization of static transmission errors of spur gears. *J Mech Des* 108(1):86–94
- Mohanty SC (2003) Tooth load sharing and contact stress analysis of high contact ratio spur gears in mesh. *J Inst Eng India* 84(2):66–70
- Wang JD, Howard I (2005) Finite element analysis of high contact ratio spur gears in mesh. *J Tribol* 127:469–483
- Sánchez MB, Pedrero JI, Pleguezuelos M (2013) Contact stress calculation of high transverse contact ratio spur and helical gear teeth. *Mech Mach Theory* 64:93–110
- Sánchez MB, Pleguezuelos M, Pedrero JI (2014) Tooth-root stress calculation of high transverse contact ratio spur and helical gears. *Meccanica* 49:347–364
- Sánchez MB, Pleguezuelos M, Pedrero JI (2017) Approximate equations for the meshing stiffness and the load sharing ratio of spur gears including hertzian effects. *Mech Mach Theory* 109:231–249
- Ye SY, Tsai SJ (2016) A computerized method for loaded tooth contact analysis of high-contact-ratio spur gears with or without flank modification considering tip corner contact and shaft misalignment. *Mech Mach Theory* 97:190–214
- Lee CW, Lin HH, Oswald FB et al (1991) Influence of linear profile modification and loading conditions on the dynamic tooth load and stress of high contact ratio gears. *J Mech Des* 113:473–480
- Lin HH, Lee CW, Oswald FB et al (1993) Computer-aided design for high-contact-ratio gears for minimum dynamic load and stress. *J Mech Des* 115:171–178
- Yildirim N, Munro RG (1999) A systematic approach to profile relief design of low and high contact ratio spur gears. *Proc Inst Mech Eng Part C* 213(6):551–562
- Yildirim N, Munro RG (1999) A new type of profile relief for high contact ratio spur gears. *Proc Inst Mech Eng Part C* 213(6):563–568
- Wang JD, Howard I (2007) A further study on high contact ratio spur gears in mesh with double scope tooth profile modification. In: *Proceedings of the ASME 2007 international design engineering technical conferences and computers and information in engineering conference*, 4–7 September 2007, Las Vegas, Nevada, USA
- Velex P, Bruyere J, Gu X (2015) An alternative approach to the definition of profile modifications in high-contact-ratio spur gears. *J Mech Des* 137(3):1–9
- Faggioni M, Samani FS, Bertacchi G (2011) Dynamic optimization of spur gears. *Mech Mach Theory* 46:544–557
- Özguven HN, Houser DR (1988) Mathematical-models used in gear dynamics: a review. *J Sound Vib* 121:383–411
- Wang JJ, Li RF, Peng XH (2003) Survey of nonlinear vibration of gear transmission systems. *Appl Mech Rev* 56(3):309–329
- Ozguven HN, Houser DR (1988) Dynamic analysis of high speed gears by using loaded static transmission error. *J Sound Vib* 125(1):71–83
- Ozguven HN (1991) A non-linear mathematical model for dynamic analysis of spur gears including shaft and bearing dynamics. *J Sound Vib* 145(2):239–260
- Kahraman A, Singh R (1990) Non-linear dynamics of a spur gear pair. *J Sound Vib* 142(1):49–75
- Kahraman A, Singh R (1991) Non-linear dynamics of a gear rotor-bearing system with multiple clearances. *J Sound Vib* 144(3):469–506
- Kahraman A, Singh R (1991) Interactions between time-varying mesh stiffness and clearances non-linearities in a geared system. *J Sound Vib* 146(1):135–156
- Blankenship GW, Kahraman A (1995) Steady state forced response of a mechanical oscillator with combined parametric excitation and clearance type nonlinearity. *J Sound Vib* 185(5):743–765
- Kahraman A, Blankenship GW (1997) Experiments on nonlinear dynamic behavior of an oscillator with clearance and periodically time-varying parameters. *J Appl Mech* 64:217–226
- Theodossiades S, Natsiavas S (2000) Non-linear dynamics of gear-pair systems with periodic stiffness and backlash. *J Sound Vib* 229(2):287–310
- Theodossiades S, Natsiavas S, Goudas I (2000) Dynamic analysis of piecewise linear oscillators with time periodic coefficients. *Int J Nonlinear Mech* 35(1):53–68
- Al-shyyab A, Kahraman A (2005) Non-linear dynamic analysis of a multi-mesh gear train using multi-term harmonic balance method: sub-harmonic motions. *J Sound Vib* 279:417–451
- Al-shyyab A, Kahraman A (2005) Non-linear dynamic analysis of a multi-mesh gear train using multi-term harmonic balance method: period-one motions. *J Sound Vib* 284:151–172
- Vaishya M, Singh R (2001) Analysis of periodically varying gear mesh systems with Coulomb friction using Floquet theory. *J Sound Vib* 243(3):525–545
- Vaishya M, Singh R (2001) Sliding friction-induced non-linearity and parametric effects in gear dynamics. *J Sound Vib* 248(4):671–694
- Velex P, Sainsot P (2002) An analytical study of tooth friction excitations in spur and helical gears. *Mech Mach Theory* 37:641–658
- He S, Gunda R, Singh R (2007) Effect of sliding friction on the dynamics of spur gear pair with realistic time-varying stiffness. *J Sound Vib* 301:927–949
- He S, Cho S, Singh R (2008) Prediction of dynamic friction forces in spur gears using alternate sliding friction formulations. *J Sound Vib* 309:843–851
- Huang K, Xiong YS, Wang T (2017) Research on the dynamic response of high-contact-ratio spur gears influenced by surface roughness under EHL condition. *Appl Surf Sci* 392:8–18
- Ma H, Song R, Pang X et al (2014) Time-varying mesh stiffness calculation of cracked spur gears. *Eng Fail Anal* 44:179–194
- Wan ZG, Cao HR, Zi YY et al (2014) An improved time-varying mesh stiffness algorithm and dynamic modeling of gear-rotor system with tooth root crack. *Eng Fail Anal* 42:157–177
- Saxena A, Parey A, Chouksey M (2016) Time varying mesh stiffness calculation of spur gear pair considering sliding friction and spalling defects. *Eng Fail Anal* 70:200–211
- Karma V, Agarwal AK (2016) Calculation of high contact ratio spur gear mesh stiffness and load sharing ratio using MATLAB & EXCEL spread sheet. *Int J Adv Res Sci Eng* 5(9):104–119
- Raghuwanshi NK, Parey A (2015) Mesh stiffness measurement of cracked spur gear by photoelasticity technique. *Measurement* 73:439–452
- Sainsot P, Velex P, Duverger O (2004) Contribution of gear body to tooth deflections—a new bidimensional analytical formula. *J Mech Des* 126(4):748–752

**Publisher's Note** Springer Nature remains neutral with regard to jurisdictional claims in published maps and institutional affiliations.